
Neural Descent for Visual 3D Human Pose and Shape

Andrei Zanfir

andreiz@google.com

Eduard Gabriel Bazavan

egbazavan@google.com

Mihai Zanfir

mihai.zanfir@google.com

William T. Freeman

wfreeman@google.com

Rahul Sukthankar

sukthankar@google.com

Cristian Sminchisescu

sminchisescu@google.com

Google Research

Abstract

We present deep neural network methodology to reconstruct the 3d pose and shape of people, given an input RGB image. We rely on a recently introduced, expressive full body statistical 3d human model, GHUM, trained end-to-end, and learn to reconstruct its pose and shape state in a self-supervised regime. Central to our methodology, is a *learning to learn and optimize* approach, referred to as HUman Neural Descent (**HUND**), which avoids *both* second-order differentiation when *training the model parameters*, and expensive *state gradient descent* in order to accurately minimize a semantic differentiable rendering loss at test time. Instead, we rely on novel recurrent stages to update the pose and shape parameters such that not only losses are minimized effectively, but the process is meta-regularized in order to ensure end-progress. **HUND**’s symmetry between training and testing makes it the first 3d human sensing architecture to natively support different operating regimes including self-supervised ones. In diverse tests, we show that **HUND** achieves very competitive results in datasets like H3.6M and 3DPW, as well as good quality 3d reconstructions for complex imagery collected in-the-wild.

1 Introduction

The rapid progress in 3D human sensing has recently relied on volumetric statistical human body models [1, 2] and supervised training. Most, if not all, state of the art architectures for predicting 2d, *e.g.*, body keypoints [3] or 3d, *e.g.*, body joints, kinematic pose and shape [4, 5, 6, 7, 8, 9, 10, 11, 12, 13, 14, 15, 16, 17, 18, 19, 20, 21, 22, 23, 24] rely, *ab initio*, at their learning core, on complete supervision. For 2d methods this primarily enters as keypoint or semantic segmentation annotations by humans, but for complex 3D articulated structures human annotation is both impractical and inaccurate. Hence for most methods, supervision comes in the form of synchronous 2d *and* 3d ground truth, mostly available in motion capture datasets like Human3.6M [25] and more recently also 3DPW [26].

Supervision-types aside, the other key ingredient of any successful system is the interplay between 3d initialization using neural networks and non-linear optimization (refinement) based on losses computed over image primitives like keypoints, silhouettes, or body part semantic segmentation maps. No existing feedforward system, particularly a *monocular* one, achieves *both* plausible 3d reconstruction *and* veridical image alignment without non-linear optimization – a key component whose effectiveness for 3d pose estimation has been long since demonstrated [27, 28].

The challenge faced by applying non-linear optimization in high-dimensional problems like 3d human pose and shape estimation stems from its complexity. On one hand, first-order model state updates are relatively inefficient for very ill-conditioned problems like *monocular* 3d human pose estimation where Hessian condition numbers in the 10^{-3} are typical [27]. Consequently, many iterations are usually necessary for good results, even when BFGS approximations are used. On the other hand, nonlinear output state optimization is difficult to integrate as part of parameter learning, since correct back-propagation would require potentially complex, computationally expensive second-order updates, for the associated layers. Such considerations have inspired some authors [7] to replace an otherwise desirable integrated learning process, with a dual system approach, where multiple non-linear optimization stages, supplying potentially improved 3d output state targets, are interleaved with classical supervised learning based on synchronized 2d and 3d data obtained by imputation. Such intuitive ideas have been shown to be effective practically, but remain expensive in training, and lack not just an explicit, integrated cost function, but also a consistent learning procedure to guarantee progress, in principle. Moreover, applying the system symmetrically, during testing, would still require potentially expensive non-linear optimization for precise image alignment.

In this paper, we take a different approach and replace the non-linear gradient refinement stage at the end of a classical 3d predictive architecture with neural descent, in a model called HUND (Human Neural Descent). In HUND, recurrent neural network stages refine the state output (in this case the 3d human pose and shape of a statistical GHUM model [2]) based on previous state estimates, loss values, and a context encoding of the input image, similarly in spirit to non-linear optimization. However, differently from models relying on gradient-based back-ends, HUND can be trained end-to-end using stochastic gradient descent, offers no asymmetry between training and testing, supports the possibility of potentially more complex, problem-dependent step updates compared to non-linear optimization, and is significantly faster. Moreover, by using such an architecture, symmetric in training and testing, with capability of refinement and self-consistency, we show, for the first time, that a 3d human pose and shape estimation system trained from monocular images can entirely bootstrap itself. The system would thus no longer necessarily require, the completely synchronous supervision, in the form of images and corresponding 3d ground truth configurations that has been previously unavoidable. Experiments in several datasets, ablation studies, and qualitative results in challenging imagery support and illustrate the main claims.

Related Work: There is considerable prior work in 3d human modeling [1, 2, 4, 5, 29, 6, 7], as well as the associated learning and optimization techniques [27, 30]. Systems combining either random 3d initialization or prediction from neural networks with non-linear optimization using losses expressed in terms of alignment to keypoints and body semantic segmentation masks exist [30, 5, 7]. Black-box optimization has gained more interest in recent years [31, 32], usually deployed in the context of meta-learning [33]. Our work is inspired in part by that of [32, 33] in which the authors introduce recurrent mechanisms to solve optimization problems, albeit in a different domain and for other representations than the ones considered in this work. [34] uses a neural network to directly regress the pose and shape parameters of a 3d body model from predicted body semantic segmentation. The network is trained in a mixed supervision regime, with either full supervision for the body model parameters or a weak supervision based on a 2d reprojection loss. [35] propose to learn a series of linear regressors over SIFT [36] features that produce descent directions analogous to an optimization algorithm for face alignment. Training is fully supervised based on 2d landmarks. Similarly, [37] learn a recurrent network, that given an input image of a face, iteratively refines face landmark predictions. The network is trained fully supervised and operates only in the 2d domain. In [38], a cascade of linear regressors are learned to refine the 3d parameters of a 3d face model. Training is done over the entire dataset at a time (multiple persons with multiple associated face images) on synthetic data, in a simulated, mixed supervision regime.

2 Methodology

We describe the elements of the proposed methodology, including the statistical 3D human body model GHUM, as well as the associated architecture used.

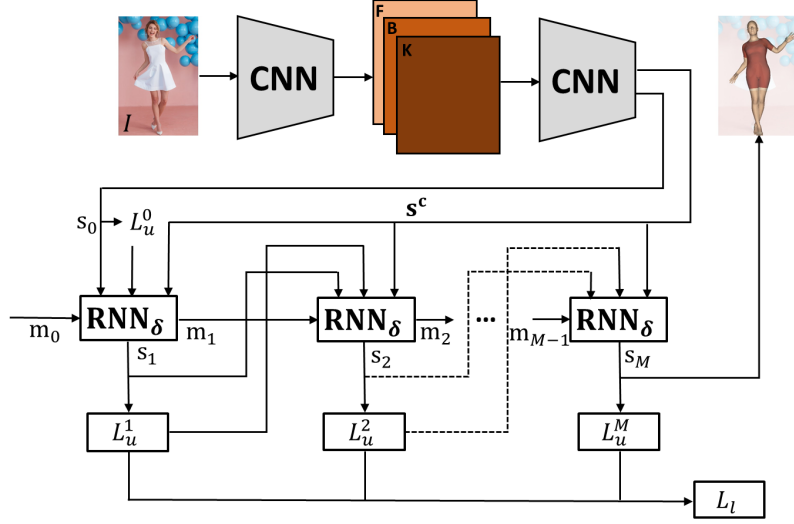


Figure 1: Overview of our Human Neural Descent (**HUND**) architecture for learning to estimate the state s of a generative human model GHUM (including shape β and pose θ , as well as person’s global rotation r and translation t) from monocular images. Given an input image, a first CNN extracts semantic feature maps for body keypoints (K) and part segmentation (B), as well as other features (F). These, in turn feed, into a second stage CNN that learns to compute a global context code s^c as well as an initial estimate of the model state s_0 . These estimates (and at later stages similar ones obtained recursively), together with the value of a semantic alignment loss L_u , expressed in terms of keypoint correspondences and differentiable rendering measures between model predictions and associated image structures, are fed into multiple refining RNN layers, with shared parameters δ , and internal memory (hidden state) m . The alignment losses (which can be unsupervised, weakly-supervised or self-supervised, depending on available data) at multiple recurrent stages M are aggregated into a learning loss L_l , optimized as part of the learning-to-learn process. The parameters are obtained using stochastic gradient descent, as typical in deep learning. The model produces refined state estimates s with precise image alignment, but does not require additional gradient calculations for the recurrent stages neither in training (e.g., second-order parameter updates), nor during testing (first-order state updates). It is also extremely efficient computationally compared to models relying on nonlinear state optimization at test time.

2.1 Statistical 3D Human Body Model GHUM

We use a recently introduced statistical 3d human body model called GHUM [2], to represent the pose and the shape of the human body. The model has been trained end-to-end, in a deep learning framework, using a large corpus of over 60,000 diverse human shapes, and 540,000 human motions, consisting of 390,000 samples from CMU and 150,000 samples from Human3.6M (subjects S1, S5, S6, S7, S8). The model has generative shape β represented using deep variational auto-encoders and generative pose θ represented using normalizing flows [39]. We assume a separable prior on the model pose and shape state $p(\theta_i, \beta_i) = p(\theta_i) + p(\beta_i)$ where Gaussian components with $\mathbf{0}$ mean and unit \mathbf{I} covariance, as typical in variational encoder and normalizing flow models. Given a monocular RGB image as input, our objective is to infer the pose $\theta \in \mathbb{R}^{N_p \times 1}$ and shape $\beta \in \mathbb{R}^{N_s \times 1}$ state variables, where N_p is the number of posing variables and N_s is the length of the shape code, respectively. A posed mesh $M(\theta, \beta)$ has N_v associated 3d vertices $\mathbf{V} = \{\mathbf{v}_i, i = 1 \dots N_v\}$ with fixed topology given by the GHUM template. Because the rigid transformation of the model in camera space – represented by a 6d rotation [40] $\mathbf{r} \in \mathbb{R}^{6 \times 1}$ and a translation vector $\mathbf{t} \in \mathbb{R}^{3 \times 1}$ – are important and require special handling, we will write them explicitly. The posed mesh thus writes $M(\theta, \beta, \mathbf{r}, \mathbf{t})$.

Camera model. We assume a pinhole camera with intrinsics $C = [f_x, f_y, c_x, c_y]^\top$ and associated perspective projection operator $\mathbf{x}_{2d} = \Pi(\mathbf{x}_{3d}, C)$, where \mathbf{x}_{3d} is any 3d point. During training and testing, intrinsics for the full input image are approximated, $f_x = W, f_y = W, c_x = W/2, c_y = H/2$, where H, W are the input dimensions. Our method works with cropped bounding-boxes of humans, re-scaled to a fixed size, of 480×480 hence we need to warp the image intrinsics C into the

corresponding crop intrinsics C_c

$$[C_c^\top 1]^\top = K[C^\top 1]^\top, \quad (1)$$

where $K \in \mathbb{R}^{5 \times 5}$ is the scale and translation matrix, adapting the image intrinsics C . By using cropped intrinsics, we effectively solve for the state of the 3d model (including global scene translation) in the camera space of the input image. For multiple detections in the same image, the resulting 3d meshes are estimated relative to a common world coordinate system, into the *same 3d scene*. At test time, when switching C_c with C , the 3d model projection will also align with the corresponding person layout in the initial image.

2.2 Learning Architecture

The network takes as input a cropped human detection and resizes it to 480×480 . A multi-stage sub-network produces features $\mathbf{F} \in \mathbb{R}^{60 \times 60 \times 256}$, keypoint detection heatmaps $\mathbf{K} \in \mathbb{R}^{60 \times 60 \times 137}$ and body-part segmentation maps $\mathbf{B} \in \mathbb{R}^{60 \times 60 \times 15}$. These are embedded into a low-dimensional space, producing a code vector \mathbf{s}^c – the superscript c stands for context, *i.e.* the optimization’s objective function context. We also append the cropped camera intrinsics C_c to this context vector. At training time, a estimate \mathbf{s}_0 of the initial GHUM state $\mathbf{s} = [\boldsymbol{\theta}^\top, \boldsymbol{\beta}^\top, \mathbf{r}^\top, \mathbf{t}^\top]^\top$ is also produced. To simulate model refinement, we employ a Recurrent Neural Network module $\text{RNN}_\delta(\mathbf{s}^c, \mathbf{s}_i, \mathbf{m}_i)$, where \mathbf{m}_i is the memory (hidden state) at refinement stage i , and unroll the updates into M stages

$$\begin{bmatrix} \mathbf{s}_i \\ \mathbf{m}_i \end{bmatrix} = \text{RNN}_\delta(\mathbf{s}_{i-1}, \mathbf{m}_{i-1}, L_u^{i-1}, \mathbf{s}^c). \quad (2)$$

The loss at each stage i is computed based on the labeling available at training time in the form of either 2d or 3d annotations. When both are missing, we are training with *self-supervision*. The self-supervised loss at each unit processing stage i can be expressed as

$$L_u^i(\mathbf{s}, \mathbf{K}, \mathbf{B}) = \lambda_k L_k(\mathbf{s}_i, \mathbf{K}) + \lambda_b L_b(\mathbf{s}_i, \mathbf{B}) + l(\boldsymbol{\theta}_i, \boldsymbol{\beta}_i), \quad (3)$$

where $l = -\log(p)$, L_k is a 2d keypoint alignment loss, L_b is a 2d semantic body part alignment (defined in terms of differentiable rendering), and M is the total number of *training* LSTM stages, while λ_k and λ_b are cross-validated scalar values which balance the loss terms.

The **keypoint alignment loss**, L_k , measures the reprojection error of the GHUM’s model 3d joints w.r.t. the predicted 2d keypoints. The loss is defined as the 2d mean-per-joint position error (MPJPE)

$$L_k(\mathbf{s}_t, \mathbf{K}) = \frac{1}{N_j} \sum_i^{N_j} \|\mathbf{j}_i(\mathbf{K}) - \Pi(\mathbf{J}_i(\mathbf{s}_t), C_c)\|_2. \quad (4)$$

with N_j keypoints, $\mathbf{j}_i(\mathbf{K})$ is the 2d location of the i -th 2d keypoint extracted from the the \mathbf{K} heatmap, and $\mathbf{J}_i(\mathbf{s}_t)$ is the i -th 3d keypoint computed by posing the GHUM model at \mathbf{s}_t .

The **body-part alignment loss**, L_b , uses the current prediction \mathbf{s}_t to create a body-part semantic segmentation image $I(\mathbf{M}(\mathbf{s}_t), C_c) \in \mathbb{R}^{H \times W \times 15}$. Then we follow a soft differentiable rasterization process[41] to fuse probabilistic contributions of all predicted mesh triangles of the model, at its current state, with respect to the rendered pixels. In this way, gradients can flow to the occluded and far-range vertices. To be able to aggregate occlusion states and semantic information, we append to each mesh vertex its semantic label, as a one-hot vector $\{0, 1\}^{15 \times 1}$, and a constant alpha value of 1. The target body part semantic probability maps \mathbf{B} are also appended with a visibility value, equal to the foreground probability $\in [0, 1]^{H \times W \times 1}$. The loss is the mean-per-pixel absolute value of the difference between the estimated and predicted semantic segmentation maps

$$L_b(\mathbf{s}_t, \mathbf{B}) = \frac{1}{HW} \sum_i^{HW} \|\mathbf{B}_i - I(\mathbf{M}(\mathbf{s}_t), C_c)_i\|_1. \quad (5)$$

For **body shape and pose**, we include two regularizers, proportional to the negative log-likelihood of their associated Gaussian distributions

$$l(\boldsymbol{\theta}) = -\log p(\boldsymbol{\theta}) = \|\boldsymbol{\theta}\|_2^2, \quad l(\boldsymbol{\beta}) = -\log p(\boldsymbol{\beta}) = \|\boldsymbol{\beta}\|_2^2. \quad (6)$$

For learning, we consider different losses L_l , including ‘sum’, ‘last’, ‘min’ or ‘max’, as follows

$$L_u^\Sigma(\mathbf{s}, \mathbf{K}, \mathbf{B}) = \sum_{i=1}^M L_u^i(\mathbf{s}_i, \mathbf{K}, \mathbf{B}), \quad L_u^\rightarrow(\mathbf{s}, \mathbf{K}, \mathbf{B}) = L_u^M(\mathbf{s}_M, \mathbf{K}, \mathbf{B}) \quad (7)$$

$$L_u^{\min}(\mathbf{s}, \mathbf{K}, \mathbf{B}) = \min_{i=1}^M L_u^i(\mathbf{s}_i, \mathbf{K}, \mathbf{B}), \quad L_u^{\max}(\mathbf{s}, \mathbf{K}, \mathbf{B}) = \max_{i=1}^M L_u^i(\mathbf{s}_i, \mathbf{K}, \mathbf{B}). \quad (8)$$

We also consider an *observable improvement* (OI) loss for L_l [33]

$$L_u^{oi} = \sum_{i=1}^M \min\{L_u^i - \min_{j < i} L_u^j, 0\}. \quad (9)$$

When 3d supervision is available, we use the following training loss $L_l = L_f^\Sigma$, as well as, potentially, the other ones previously introduced in (7) for the self-supervised regime

$$L_f^\Sigma(\mathbf{s}) = \sum_{i=1}^M \left[\lambda_m L_m(\mathbf{M}(\mathbf{s}_i), \widetilde{\mathbf{M}}) + l(\boldsymbol{\theta}_i, \boldsymbol{\beta}_i) \right], \quad (10)$$

where L_m represents the 3d vertex error between the ground-truth mesh $\widetilde{\mathbf{M}}$ and a predicted one, $\mathbf{M}(\mathbf{s}_i)$ – obtained by posing the GHUM model using the predicted state \mathbf{s}_i .

3 Experiments

View of Experimental Protocols. There is large variety of models and methods now available for 3d human sensing research, including body models like SMPL [1] and GHUM [2], or reconstruction methods like DMHS [4], HMR [6], SPIN [7] *etc.*, set aside methods that combine random initialization or neural network prediction and non-linear refinement[30, 42]. To make things even more complex, some models are pre-trained on different 2d or 3d datasets and refined on others. A considerable part of this development has a historical trace, with models built on top of each-other and inheriting their structure and training sets, as available at different moments in time. Set that aside, multiple protocols are used for testing. For Human3.6M [25] only, there are at least 4: the ones originally proposed by the dataset creators, on the withheld test set of Human3.6M (or the representative subset Human80K [43]) as well as others, created by various authors, known as protocol 1 and 2 by re-partitioning the original training and validation sets for which ground truth is available. Out of these 2, only protocol 1 is sufficiently solid in the sense of providing a reasonably large and diverse test set for stable statistics (*e.g.*, 110,000 images from different views in P1 vs. 13,700 in P2, from the same camera, at the same training set size of 312,000 configurations for both). Hence we use P1 here. We will also use 3DPW [26] for similar reasons, or rather, in the absence of other options in the wild (30,150 training and 33,000 testing configurations). Testing all other model combinations would be both impractical and irrelevant, especially for new models like GHUM where most prior combinations are unavailable and impossible to replicate. As a matter of principle, reconstruction models can be evaluated based on the amount of supervision received, be it **#2d**, **# 3d**, or synchronized **#2d-3d** annotations, the number of images used for self-supervision **#I**, as well as perhaps number of parameters and run-time. In addition, ablations for each model, *e.g.*, **HUND**, would offer insights into different components and their relevance. We argue in support of this being one scientifically sound way of promoting diversity in the creation of new models and methods, rather than closing towards premature methodological convergence, weakly supported by unsustainable, ad-hoc, experimental combinatorics.

For our **self-supervised (SS)** experiments, we employ two datasets containing images in-the-wild, COCO2017 [44] (30,000 images) and OpenImages [45] (24,000), with no annotations in training and testing. We refer to **weakly-supervised (WS)** experiments as those where ground truth annotations are available, *e.g.* human body keypoints. We do not rely on these but some other techniques including HMR and SPIN do, hence we make this distinction in order to correctly reflect their supervision level.

For **fully supervised (FS)** experiments, we employ H3.6M and 3DPW. Because we work with the newly released GHUM model, we retarget the mocap raw marker data from H3.6M to obtain accurate 3d mesh supervision for our model [2]. Because the ground-truth of 3DPW is provided as SMPL 3d meshes, we fit the GHUM model by using an objective function minimizing vertex-to-vertex distances between the two corresponding meshes.

Architecture Implementation. To predict single-person keypoints and body part segmentation, we train a multi-task network with ResNet50 [46] backbone (the first CNN in our pipeline, see fig.1)[4]. We have 137 2d keypoints as in [47] and 15 body part labels, as in [48]. This network has 34M trainable parameters. The self-supervised training protocol for **HUND** assumes only images are available and we predict 2d body keypoints and body part labels during training, in addition to body shape and pose regularizers. For the embedding model (the second CNN in the pipeline) predicting s^c , we use a series of 6 convolutional layers with pooling, followed by a fully connected layer. We use $M = 5$ LSTM [49] stages as RNNs for **HUND** and we set the number of units to 256, which translates to 525k parameters. In total there are 950k trainable parameters for the 3D reconstruction model. We train with a batch size of 32 and a learning rate of 10^{-4} for 50 epochs. For experiments where we train HUND using **FS+SS**, we use a mixed schedule, alternating between self-supervised and fully-supervised batches. Training takes about 72 hours on a single Nvidia Tesla P100 GPU. The runtime of our prediction network for a single image is 0.035s and 0.02s for **HUND**, on an Nvidia RTX 2080 GPU.

Method	MPJPE-PA	MPJPE	MPJPE Trans	#2d	#3d	#2d-3d	#I
HMR (FS+WS) [6]	58.1	88.0	NR	111k	720k	300k	0
SPIN (FS+WS) [7]	NR	NR	NR	111k	720k/390k	300k	0
HUND (FS+SS)	53.0	72.0	160.0	0	540k	150k	54k
HMR (WS) [6]	67.45	106.84	NR	111k	720k	0	0
HUND (SS)	66.0	102.0	175.0	0	540k	0	54k

Table 1: Performance of different pose and shape estimation methods on the H3.6M dataset, with training/testing based on the representative protocol P1 (for self-supervised variants this only indicates the images used in testing). MPJPE-PA and MPJPE are expressed in mm. We also report the global translation of the body as this is supported by our fully perspective camera model (N.B. this is not supported by other methods which use an orthographic perspective model). We also compare different annotations used in the construction of different models, with a split into 2d, 3d and synchronized 2d-3d. The last column gives the number of images for self-supervised variants, *e.g.*, HUND(SS), which do not use either 2d image keypoints or synchronized images and 3d mocap during training.

Method	MPJPE-PA (mm)	MPJPE (mm)
HMR (FS+WS) [6]	81.3	103.8
SPIN (FS+WS)[7]	59.2	96.9
HUND (SS)	70.3	98.1
HUND (FS+SS)	56.5	87.7

Table 2: Results on the 3DPW test set for different methods. Notice that a self-supervised version of HUND produces lower errors compared to the best supervised HMR implementation that includes not just synchronized 2d–3d training sets but also images with 2d annotation ground truth. A HUND model that includes asynchronous 2d-3d supervision, in addition to just unlabeled images, achieves the lowest error, and uses less training data than any other competitive method – see also table 1.

Evaluation and discussion. Multiple experiments are run for different regimes. Quantitative results are presented in tables 1 and 2 for Human3.6M and 3DPW respectively. A detailed analysis of optimization behavior for one image is given in fig. 2 as well as, in aggregate, in fig. 3. Visual reconstructions at different HUND optimization stages, for several images, are given in fig. 5. We also study the impact of different training losses, as given in (7) and (9), on the quality of results of HUND. We use a HUND (FS) model trained and evaluated on Human3.6M (protocol 1). From table 3 we observe that the last (L_f^\rightarrow) and sum (L_f^Σ) losses perform best, whereas others produce considerably less competitive results, by some margin, for this problem.

Finally, we show qualitative visual 3d reconstruction results, from several viewpoints, for a variety of difficult poses and backgrounds in fig. 4. *Please see our Sup. Mat. for videos!*

4 Conclusions

We have presented a neural model, **HUND**, to reconstruct the 3d pose and shape of people from image data. In doing so, we rely on an expressive full body statistical 3d human model, GHUM, to

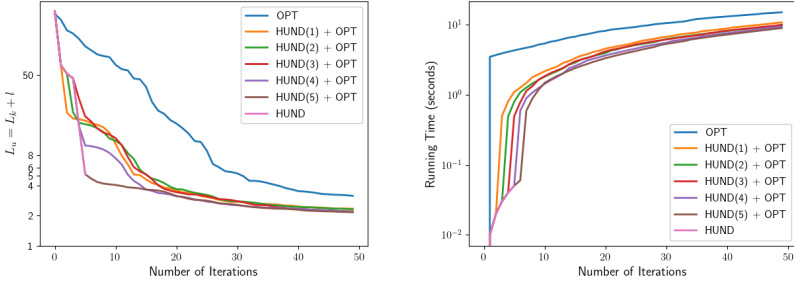


Figure 2: Behavior of different optimization methods including standard non-linear gradient-based BFGS, HUND(5), as well as variants of HUND(i), $i \leq 5$, initializing BFGS, in order to assess progress and the quality of solutions obtained along the way (left). Corresponding cumulative run-times are shown on the right. Observe that HUND produces a good quality solution orders of magnitude faster than gradient descent (note log-scales on both plots). End refinement using gradient descent improves results, although we do not recommend a hybrid approach—here we only show different hybrids for insight. This shows one optimization trace for a model initialized in A-pose and estimated given one image from Human3.6M, but such behavior is typical of aggregates, see *e.g.*, fig. 3. See also fig. 5 for visual illustrations of different configurations sampled by HUND during optimization.

Loss	MPJPE-PA (mm)	MPJPE (mm)
L_f^{\rightarrow}	58.50	80.16
L_f^{Σ}	59.91	83.26
L_f^{\min}	78.61	122.60
L_f^{oi}	79.35	123.90
L_f^{\max}	83.80	128.0

Table 3: Impact assessment of different meta-losses used in HUND (FS), trained on the Human3.6M dataset, following protocol 1. The last and sum losses perform similarly well, with others following at distance.

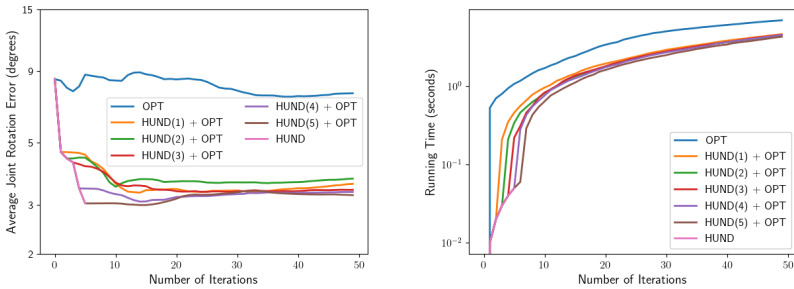


Figure 3: Optimization statistics for different methods, aggregated over 100 different poses (estimation runs) from Human3.6M. We initialize in an A-pose and perform monocular 3d pose and shape reconstruction for GHUM under a HUND (FS+SS) model, as well as non-linear optimization baselines. On the left we show per-joint angle averages w.r.t. ground truth. On the right we show running times in aggregate for different types of optimization. One can see that BFGS descent under a keypoint+prior loss tends to be prone to inferior local optima compared to different HUND hybrids, which on average find significantly better solutions. The plot needs to be interpreted in proper context, as aggregates meant to show distance and run-time statistics per iteration. Hence, they may not be entirely representative of any single run, but for a singleton see *e.g.*, fig. 2.

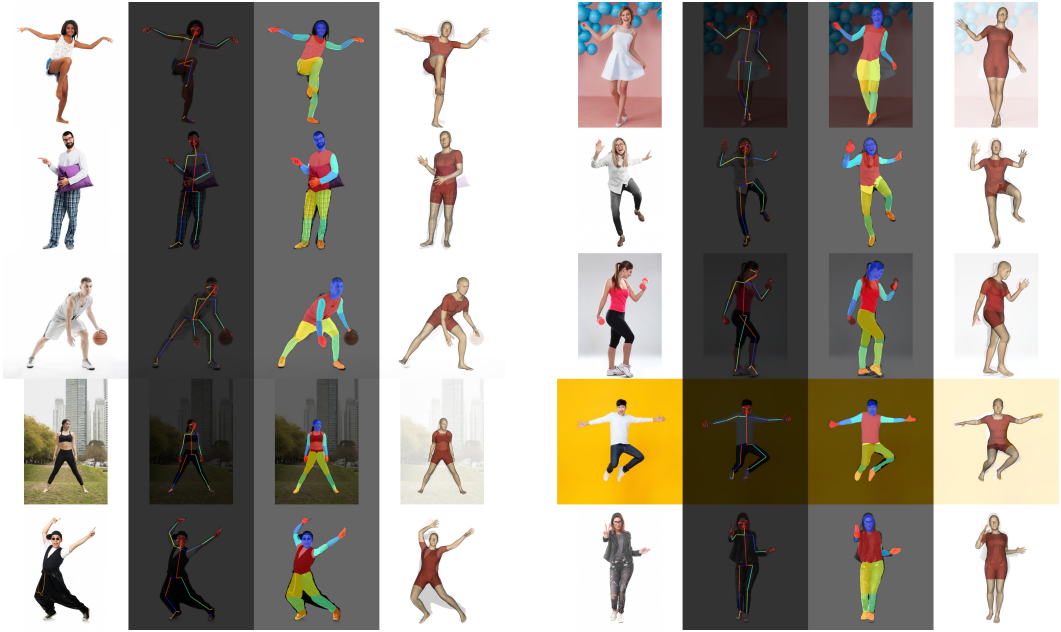


Figure 4: Visual 3d reconstruction results obtained by **HUND**. Given initial 2d predictions for body, face and hand keypoints, and initial predictions for semantic body part labelling, the neural descent network predicts the 3d GHUM pose and shape parameters. Best seen in color. For other examples and videos see our Sup. Mat.

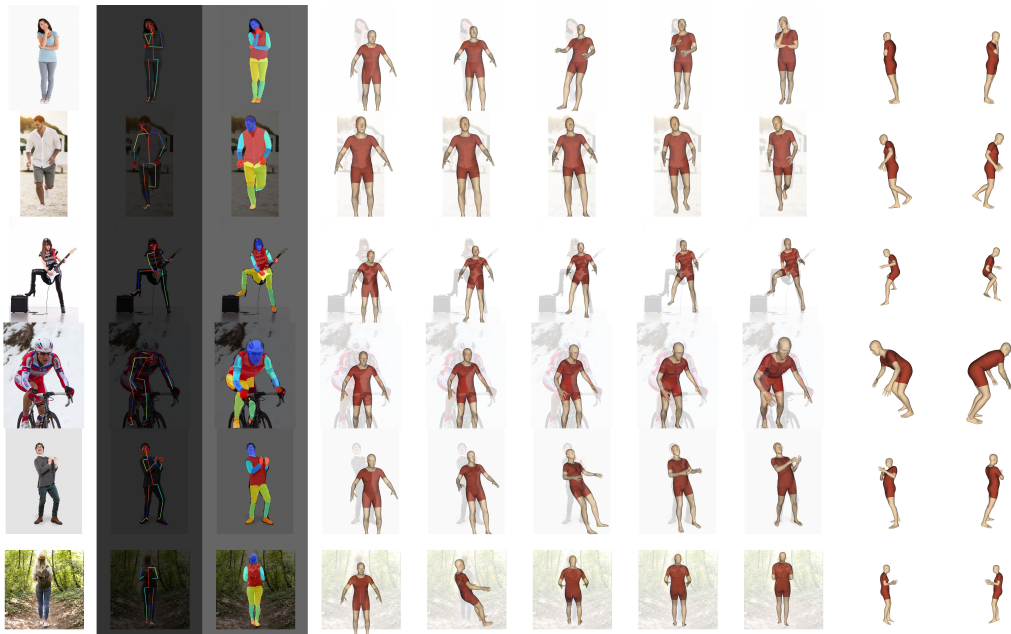


Figure 5: Visual 3d pose and shape configurations of GHUM sampled by **HUND** during optimization. First column shows the input image, columns 3 and 3 illustrate 2d keypoint detections and semantic body parts segmentations estimated by the model. Columns 4-8 illustrate GHUM estimates at each HUND stage. Columns 9 and 10 show visualizations of the GHUM state from different viewpoints, after HUND terminates.

capture typical human shape and motion regularities. Even so, accurate reconstruction and continuous learning are challenging because large-scale diverse 3d supervision is difficult to acquire for people, and because the most efficient inference is typically based on non-linear state alignment. This is however difficult to correctly ‘supra’-differentiate, to second order, in training and expensive in testing. To address such challenges, we rely on self-supervision based on differentiable rendering within *learning-to-learn* approaches based on recurrent networks, which avoid expensive gradient descent in testing, yet provide a surrogate for robust loss minimization. **HUND** is tested and achieves very competitive results for datasets like H3.6M and 3DPW, as well as for complex poses, collected in challenging outdoor conditions. HUND’s learning-to-learn capabilities, and symmetry between training and testing, can make it the first architecture to demonstrate the possibility of bootstrapping a plausible 3d human reconstruction model without initial, synchronous (2d, 3d) supervision.

5 Appendix

CNN Semantic Feature Extraction Network. The semantic feature extraction network for 2d keypoints and body parts was trained on a subset of OpenImages which was annotated with 2d keypoints and body part labelling. For augmentation we used translation, cropping, rotations and flipping. As described in the paper we use a ResNet50 [46] backbone. The bottleneck layers of the backbone are passed through deconvolution layers, resized to a common size and concatenated to a final tensor used to store the feature maps \mathbf{F} . The feature maps are used to create separate heads, one for keypoints \mathbf{K} and another one for body parts \mathbf{B} . During training, we first learn the weights for $\mathbf{F} + \mathbf{K}$, then we freeze the weights for \mathbf{F} and learn the weights for \mathbf{B} . While training the weights for the 3d component of **HUND** (second CNN in fig. 1), the weights for \mathbf{F} , \mathbf{K} and \mathbf{B} are frozen.

Perspective Model and Virtual Camera Crops. This section describes our perspective camera model which allows us to plausibly place the GHUM’s 3d reconstructions in the scene (as opposed to just showing them overlayed with input images, or in a person-centered coordinate system). This involves several sub-steps including an adequate initialization for GHUM, as well as the process to properly transfer between the native camera coordinate system where the image was captured and a crop’s coordinate system and associated virtual camera model of the human detection.

First, we describe the details for computing the initial GHUM state $\mathbf{s}_0 = [\theta_0^\top, \beta_0^\top, \mathbf{r}_0^\top, \mathbf{t}_0^\top]^\top$ (see line 117 in the paper).

We set $\theta_0 = \mathbf{0}$, $\beta_0 = \mathbf{0}$, $\mathbf{r}_0 = [-1, 0, 0, -1, 0, 0]^\top$, values which effectively place the model in an upright position, with the average statistical body shape and pose. For estimating the initial translation \mathbf{t}_0 one needs to take into consideration the camera intrinsics (N.B. this initialization will only be used in order to handle the transformation from the full camera model to a virtual model associated to the crop associated to a human detection).

Our camera model assumes either that camera intrinsics $C = [f_x, f_y, c_x, c_y]^\top$ are known, or default values $f_x = W, f_y = H, c_x = W/2, c_y = H/2$ are used, where H, W are the input dimensions. Given image intrinsics C one has to compute the corresponding crop intrinsics C_c (see line 104 in paper). The crop intrinsics C_c vary depending on the input: we compute an initial translation \mathbf{t}_0 such that the initially reconstructed GHUM mesh projects centrally in the image.

We consider a default set of 2d joint positions \mathbf{J}_d in the crop image which is always of size 480×480 . We compute \mathbf{J}_d by projecting the default model given some default intrinsics $C_d = [480, 480, 240, 240]^\top$ and placing the subject e.g. 2 meters in front of the camera. Since we work with an A-pose, the body joints will all project inside the initial crop and tightly bounded within its borders.

We then minimize the following objective using e.g. least squares and obtain \mathbf{t}_0

$$\mathbf{t}_0 = \arg \min_{\mathbf{t}} \|\mathbf{J}_d - \Pi(\mathbf{J}(\theta_0, \beta_0, \mathbf{r}_0, \mathbf{t}), C_c)\|_2. \quad (11)$$

where $\Pi(\mathbf{J}(\theta_0, \beta_0, \mathbf{r}_0, \mathbf{t}), C_c)$ are the GHUM model joints viewed under a perspective projection using the C_c crop intrinsics.

Rotation angles computation. We describe the details for computing the angles reported in fig. 3. Given rotation matrices for 2 corresponding joints \mathbf{R}_1 and \mathbf{R}_2 , we compute their difference as $\mathbf{R}_1 \mathbf{R}_2^\top$. The angle associated to the rotation difference is then obtained using the formula $\arccos \frac{\text{Tr}(\mathbf{R}_1 \mathbf{R}_2^\top) - 1}{2}$.

Broader Impact

Automatic 3d human sensing from images and video would be a key, transformative enabler in areas as diverse as clothing virtual apparel try-on, fitness, personal well-being, health or rehabilitation, AR and VR for improved communication or collaboration, self-driving systems with emphasis to urban scenarios, special effects, human-computer interaction or gaming, among others. Applications in shopping, telepresence or fitness would increase human engagement and stimulate both collaboration and communication, and the economy, during a lock-down.

The methodology we describe aims to decrease bias by introducing flexible forms of self-supervision which would allow system bootstrapping and adaptation to new domains and subject distributions for which labeled data may be difficult or impossible to collect upfront. In contrast, applications like visual surveillance and person identification would not be effectively supported currently, given that model’s output does not provide sufficient detail or resolution for these purposes. The same is true for the creation of potentially adversely-impacting deepfakes, as an appearance model or a joint audio-visual model are not included to support photorealistic visual and voice synthesis.

References

- [1] M. Loper, N. Mahmood, J. Romero, G. Pons-Moll, and M. J. Black, “SMPL: A skinned multi-person linear model,” *SIGGRAPH*, 2015.
- [2] H. Xu, E. G. Bazavan, A. Zanfir, B. Freeman, R. Sukthankar, and C. Sminchisescu, “GHUM & GHUML: Generative 3D human shape and articulated pose models,” *CVPR*, 2020.
- [3] Z. Cao, T. Simon, S.-E. Wei, and Y. Sheikh, “Realtime multi-person 2d pose estimation using part affinity fields,” in *CVPR*, 2017.
- [4] A. Popa, M. Zanfir, and C. Sminchisescu, “Deep Multitask Architecture for Integrated 2D and 3D Human Sensing,” in *CVPR*, 2017.
- [5] A. Zanfir, E. Marinoiu, and C. Sminchisescu, “Monocular 3d pose and shape estimation of multiple people in natural scenes—the importance of multiple scene constraints,” in *CVPR*, 2018.
- [6] A. Kanazawa, M. J. Black, D. W. Jacobs, and J. Malik, “End-to-end recovery of human shape and pose,” in *CVPR*, 2018.
- [7] N. Kolotouros, G. Pavlakos, M. J. Black, and K. Daniilidis, “Learning to reconstruct 3d human pose and shape via model-fitting in the loop,” in *Proceedings of the IEEE International Conference on Computer Vision*, pp. 2252–2261, 2019.
- [8] Y. Sun, Y. Ye, W. Liu, W. Gao, Y. Fu, and T. Mei, “Human mesh recovery from monocular images via a skeleton-disentangled representation,” in *Proceedings of the IEEE International Conference on Computer Vision*, pp. 5349–5358, 2019.
- [9] C. Doersch and A. Zisserman, “Sim2real transfer learning for 3d human pose estimation: motion to the rescue,” in *Advances in Neural Information Processing Systems*, pp. 12929–12941, 2019.
- [10] A. Kanazawa, J. Y. Zhang, P. Felsen, and J. Malik, “Learning 3d human dynamics from video,” in *Computer Vision and Pattern Recognition (CVPR)*, 2019.
- [11] N. Kolotouros, G. Pavlakos, and K. Daniilidis, “Convolutional mesh regression for single-image human shape reconstruction,” in *Proceedings of the IEEE Conference on Computer Vision and Pattern Recognition*, pp. 4501–4510, 2019.
- [12] A. Arnab, C. Doersch, and A. Zisserman, “Exploiting temporal context for 3d human pose estimation in the wild,” 2019.
- [13] Y. Xu, S.-C. Zhu, and T. Tung, “Denserac: Joint 3d pose and shape estimation by dense render-and-compare,” in *Proceedings of the IEEE International Conference on Computer Vision*, pp. 7760–7770, 2019.
- [14] M. Kocabas, N. Athanasiou, and M. J. Black, “Vibe: Video inference for human body pose and shape estimation,” *CVPR*, 2020.
- [15] G. Varol, D. Ceylan, B. Russell, J. Yang, E. Yumer, I. Laptev, and C. Schmid, “BodyNet: Volumetric inference of 3D human body shapes,” in *ECCV*, 2018.

- [16] A. S. Jackson, C. Manafas, and G. Tzimiropoulos, “3d human body reconstruction from a single image via volumetric regression,” in *ECCV*, 2018.
- [17] G. Pavlakos, X. Zhou, K. G. Derpanis, and K. Daniilidis, “Coarse-to-fine volumetric prediction for single-image 3d human pose,” in *CVPR*, 2017.
- [18] W. Yang, W. Ouyang, X. Wang, J. Ren, H. Li, and X. Wang, “3d human pose estimation in the wild by adversarial learning,” in *CVPR*, 2018.
- [19] X. Zhou, Q. Huang, X. Sun, X. Xue, and Y. Wei, “Towards 3d human pose estimation in the wild: a weakly-supervised approach,” in *ICCV*, 2017.
- [20] G. Rogez and C. Schmid, “Mocap-guided data augmentation for 3d pose estimation in the wild,” in *NeurIPS*, 2016.
- [21] B. Tekin, P. Marquez Neila, M. Salzmann, and P. Fua, “Learning to fuse 2d and 3d image cues for monocular body pose estimation,” in *ICCV*, 2017.
- [22] D. Mehta, S. Sridhar, O. Sotnychenko, H. Rhodin, M. Shafiei, H.-P. Seidel, W. Xu, D. Casas, and C. Theobalt, “Vnect: Real-time 3d human pose estimation with a single rgb camera,” *ACM Transactions on Graphics (TOG)*, 2017.
- [23] J. Martinez, R. Hossain, J. Romero, and J. J. Little, “A simple yet effective baseline for 3d human pose estimation,” in *ICCV*, 2017.
- [24] K. Iskakov, E. Burkov, V. Lempitsky, and Y. Malkov, “Learnable triangulation of human pose,” in *International Conference on Computer Vision (ICCV)*, 2019.
- [25] C. Ionescu, D. Papava, V. Olaru, and C. Sminchisescu, “Human3.6M: Large scale datasets and predictive methods for 3d human sensing in natural environments,” *PAMI*, 2014.
- [26] T. von Marcard, R. Henschel, M. Black, B. Rosenhahn, and G. Pons-Moll, “Recovering accurate 3d human pose in the wild using IMUs and a moving camera,” in *ECCV*, 2018.
- [27] C. Sminchisescu and B. Triggs, “Estimating Articulated Human Motion with Covariance Scaled Sampling,” *IJRR*, vol. 22, no. 6, pp. 371–393, 2003.
- [28] C. Sminchisescu and B. Triggs, “Kinematic jump processes for monocular 3d human tracking,” in *CVPR*, 2003.
- [29] H. Rhodin, M. Salzmann, and P. Fua, “Unsupervised geometry-aware representation for 3d human pose estimation,” in *ECCV*, September 2018.
- [30] F. Bogo, A. Kanazawa, C. Lassner, P. Gehler, J. Romero, and M. J. Black, “Keep it SMPL: Automatic estimation of 3d human pose and shape from a single image,” in *ECCV*, 2016.
- [31] M. Andrychowicz, M. Denil, S. Gomez, M. W. Hoffman, D. Pfau, T. Schaul, B. Shillingford, and N. De Freitas, “Learning to learn by gradient descent by gradient descent,” in *NeurIPS*, pp. 3981–3989, 2016.
- [32] Y. Chen, M. W. Hoffman, S. G. Colmenarejo, M. Denil, T. P. Lillicrap, M. Botvinick, and N. De Freitas, “Learning to learn without gradient descent by gradient descent,” in *ICML*, pp. 748–756, 2017.
- [33] T. Hospedales, A. Antoniou, P. Micaelli, and A. Storkey, “Meta-learning in neural networks: A survey,” 2020.
- [34] M. Omran, C. Lassner, G. Pons-Moll, P. V. Gehler, and B. Schiele, “Neural body fitting: Unifying deep learning and model-based human pose and shape estimation,” in *3DV*, 2018.
- [35] X. Xiong and F. De la Torre, “Supervised descent method and its applications to face alignment,” in *CVPR*, pp. 532–539, 2013.
- [36] D. G. Lowe, “Distinctive image features from scale-invariant keypoints,” *International journal of computer vision*, vol. 60, no. 2, pp. 91–110, 2004.
- [37] G. Trigeorgis, P. Snape, M. A. Nicolaou, E. Antonakos, and S. Zafeiriou, “Mnemonic descent method: A recurrent process applied for end-to-end face alignment,” in *CVPR*, pp. 4177–4187, 2016.
- [38] W. Tian, F. Liu, and Q. Zhao, “Regressing 3d face shapes from arbitrary image sets with disentanglement in shape space,” in *2019 International Conference on Biometrics (ICB)*, pp. 1–7, IEEE, 2019.

- [39] A. Zanfir, E. G. Bazavan, H. Xu, B. Freeman, R. Sukthankar, and C. Sminchisescu, “Weakly supervised 3d human pose and shape reconstruction with normalizing flows,” *arXiv preprint arXiv:2003.10350*, 2020.
- [40] Y. Zhou, C. Barnes, J. Lu, J. Yang, and H. Li, “On the continuity of rotation representations in neural networks,” *arXiv preprint arXiv:1812.07035*, 2018.
- [41] S. Liu, T. Li, W. Chen, and H. Li, “Soft rasterizer: A differentiable renderer for image-based 3d reasoning,” *arXiv preprint arXiv:1904.01786*, 2019.
- [42] A. Zanfir, E. Marinoiu, and C. Sminchisescu, “Monocular 3D Pose and Shape Estimation of Multiple People in Natural Scenes – The Importance of Multiple Scene Constraints,” in *CVPR*, 2018.
- [43] C. Ionescu, J. Carreira, and C. Sminchisescu, “Iterated second-order label sensitive pooling for 3d human pose estimation,” in *CVPR*, 2014.
- [44] T.-Y. Lin, M. Maire, S. Belongie, J. Hays, P. Perona, D. Ramanan, P. Dollár, and C. L. Zitnick, “Microsoft coco: Common objects in context,” in *ECCV*, 2014.
- [45] A. Kuznetsova, H. Rom, N. Alldrin, J. Uijlings, I. Krasin, J. Pont-Tuset, S. Kamali, S. Popov, M. Malloci, T. Duerig, and V. Ferrari, “The open images dataset v4: Unified image classification, object detection, and visual relationship detection at scale,” *arXiv:1811.00982*, 2018.
- [46] K. He, X. Zhang, S. Ren, and J. Sun, “Identity mappings in deep residual networks,” in *ECCV*, pp. 630–645, Springer, 2016.
- [47] Z. Cao, G. M. Hidalgo, T. Simon, S. Wei, and Y. Sheikh, “Openpose: Realtime multi-person 2d pose estimation using part affinity fields.,” *PAMI*, 2019.
- [48] I. K. Riza Alp Guler, Natalia Neverova, “Densepose: Dense human pose estimation in the wild,” *arXiv*, 2018.
- [49] S. Hochreiter and J. Schmidhuber, “Long short-term memory,” *Neural computation*, vol. 9, no. 8, pp. 1735–1780, 1997.